Materials Today Energy 47 (2025) 101741

Contents lists available at ScienceDirect

Materials Today Energy

journal homepage: www.journals.elsevier.com/materials-today-energy/

Double-side integration of the fluorinated self-assembling monolayers for enhanced stability of inverted perovskite solar cells

Ekaterina A. Ilicheva [a,1], Polina K. Sukhorukova [a,b,1], Lev O. Luchnikov [a], Dmitry O. Balakirev [b], Nikita S. Saratovsky [b], Andrei P. Morozov [a], Pavel A. Gostishchev [a], Sergey Yu. Yurchuk [c], Anton A. Vasilev [c], Sergey S. Kozlov [d], Sergey I. Didenko [c], Svetlana M. Peregudova [b,e], Dmitry S. Muratov [f], Yuriy N. Luponosov [b,*], Danila S. Saranin [a,**]

[a] LASE – Laboratory of Advanced Solar Energy, National University of Science and Technology "MISiS", Leninsky Prospect 4, 119049, Moscow, Russia
[b] Enikolopov Institute of Synthetic Polymeric Materials of the Russian Academy of Sciences (ISPM RAS), Profsoyuznaya St. 70, Moscow, 117393, Russia
[c] Department of Semiconductor Electronics and Semiconductor Physics, National University of Science & Technology MISIS, 4 Leninsky Ave., Moscow, 119049, Russia
[d] Laboratory of Solar Photoconverters, Emanuel Institute of Biochemical Physics, Russian Academy of Sciences, 119334, Moscow, Russia
[e] A.N. Nesmeyanov Institute of Organoelement Compounds of the Russian Academy of Sciences, Vavilova St. 28, Moscow, 119991, Russia
[f] Department of Chemistry, University of Turin, 10125, Turin, Italy

ARTICLE INFO

Keywords:
Self-assembling monolayers
Surface passivation
Perovskite solar cells
Conjugated triphenylamine-based molecules

ABSTRACT

Traps and structural defects at the hole and electron transport interfaces of the microcrystalline absorber limits the efficiency and long-term stability of perovskite solar cells (PSCs) due to accumulation of the ionic clusters, non-radiative recombination and electrochemical corrosion. Surface engineering using self-assembled monolayers (SAM) was considered as an effective strategy for modification of charge-collection junctions. In this work, we demonstrate the first report about complex integration of a SAM for double-side passivation in p-i-n PSCs. Integrating the novel 5-(4-[*bis*(4-fluorophenyl)amino]phenyl)thiophene-2-carboxylic acid (FTPATC) as a fluorinated SAM at the hole-transport interface reduced potential barriers and lattice stresses in the absorber. At the electron-transport side, FTPATC interacted with the A-site cations of the perovskite molecule (Cs, formamidinium), inducing a dipole for defect compensation. Using the passivation approach with fluorinated SAM demonstrated benefits in the gain of the output performance up to 22.2 %. The key-advantage of double-side passivation was confirmed by the enhanced stability under continuous light-soaking (1-sun equivalent, 65 °C, ISOS-L-2), maintaining 88 % of the initial performance over 1680 h and thermal stabilization under harsh heating at 90 °C.

1. Introduction

Halide perovskites (**HPs**) stand out as one of the most promising materials for next-generation photovoltaics (**PVs**) [1], owing unique combination of semiconductor properties and simplified fabrication technology. Solar cells based on HPs are thin-film devices with an absorber of submicron thickness and microcrystalline morphology. HP layers are characterized by strong absorption in the visible range (10^4–10^5 cm^{-1}) [2], suppressed non-radiative recombination dynamics [3], and relatively high charge carrier mobility (up to 10 cm^2 V^{-1} s^{-1}) [4]. Combined with scalable manufacturing methods based on solution-processing (slot-die coating [5], ink-jet printing [6], etc.), this technology shows great potential for reducing capital expenditures (**CAPEX**) at the commercialization stage [7]. To date, perovskite solar cells (**PCSs**) have achieved a power conversion efficiency (**PCE**) record of 26.7 % [8], demonstrating benefits over well-developed PV technologies compared to thin-film CdTe and CIGS devices, and offering competitive performance with various crystalline Si cells [8].

However, the use of simplified technological processes complicates the fine-tuning of transport properties and the structural perfection of HP thin-films. Microcrystalline absorber interfaces are characterized with uncompensated defects and a high concentration of structural

* Corresponding author.
** Corresponding author.
E-mail addresses: luponosov@ispm.ru (Y.N. Luponosov), saranin.ds@misis.ru (D.S. Saranin).
[1] The authors contributed equally to this work.

https://doi.org/10.1016/j.mtener.2024.101741
Received 8 August 2024; Received in revised form 25 October 2024; Accepted 14 November 2024
Available online 15 November 2024

imperfections [9]. The presence of ionic species and perovskite decomposition products (I_2, etc.) [10] can induce unfavorable accumulation at the contacts with transport layers or electrodes under an electric field [11], potentially triggering electrochemical corrosion. This can result in the decomposition of perovskite and the degradation of the device structure.

The interface engineering using self-assembled monolayers (SAM) was considered as an effective strategy for surface passivation and improvement of energy level alignment in PSCs. The formation of SAM is made possible by the phenomenon of self-assembly, which refers to the spontaneous organization of components into patterns and structures [12]. The formation of SAM is contingent upon the availability of a range of interactions, including covalent bonds, hydrogen bonding, electrostatic interactions, hydrophobic interactions, and steric repulsion between the SAM matrix and the substrate material [13]. The formation of covalent bonds in semiconductor devices between SAM and materials employed in electrodes and transport layers (for example, metal oxides) is feasible due to the presence of the so-called anchor group in the SAM. It is most common for acid residues to act as anchor groups, specifically carboxylic and organophosphorus acids. Covalent bonds are formed between the oxygen or hydrogen atoms of the acid group and the metal or oxygen atoms of the semiconductor material [14].

To achieve the optimal properties of SAM, it is possible to vary the anchor group and modify the terminal group of the molecule. A common method for modifying SAM is the introduction of halogen atoms into the terminal group. The incorporation of F, Cl, Br, or I into the molecular composition allows for the manipulation of HOMO and LUMO levels, the work function ($\mathbf{W_F}$), the hydrophobicity of the resulting material's surface [15], and consequently, the photovoltaic properties of the final device. Of the halogens, the modification of SAM by the introduction of a fluorine atom into the molecule is particularly noteworthy. The fluorine atom is notable for its strong electronegativity, which enables it to form robust hydrogen bonds with the hydrogens of the amino groups present in the organic ligands of the perovskite. This binding action increases the thermal stability of the device. Furthermore, the surfaces formed by fluorinated molecules are typically hydrophobic, providing a protective barrier against moisture-induced erosion [16].

In the actual literature, numerous reports highlight the advantages for application of SAM for hole-transport interlayers, mainly in p-i-n device architectures [17]. However, surface passivation and stabilization at the absorber/charge transport layer junction on the electron collection side are also required. Double-side passivation, close to c-Si/amorphous-Si heterostructures concept [18], represents a promising approach for stabilization of interfaces and improvement in charge collection efficiency. Several research groups reported the efforts for double side interface modification using organic dielectrics [19], polyelectrolytes [20], halide-containing compounds [21] and 2D perovskites [22]. Nevertheless, the stabilization of interfaces and improvements in device efficiency necessitate the development of novel methods and their implementation. The subject of integrating double-sided passivation with modified self-assembled monolayers (SAMs) has yet to undergo rigorous investigation and analysis. In this paper we present a comprehensive study on the use of self-assembled monolayer based on 5-(4-[*bis*(4-fluorophenyl)amino]phenyl)thiophene-2-carboxylic acid (FTPATC) for both-side interface passivation in p-i-n PSC. In our recent research [23], we demonstrated devices based on TPATC material that exhibited excellent performance. To further enhance the material, TPATC underwent a modification process involving the introduction of two fluorine atoms into the benzene rings of the triphenylamine unit, situated in the para-position relative to the nitrogen atom.

We presented a complex investigation into the effect of FTPATC on the surface and optoelectronic properties of the double-cation perovskite $CsFAPbI_{2.93}Cl_{0.07}$. SAM integration resulted in significant Fermi level pinning, changes in energy level alignment, and qualitative improvements in buried interface morphology. We found that FTPATC suppresses trapping and reduces non-radiative recombination, which in turn decreased the dark currents and the non-ideality factor of the PSCs. Passivation with SAM gained the photoelectric performance from ~20 % for the bare device to ~22 % for p-side modification and ~21 % for double-side configuration, respectively. Interface engineering with FTPATC allowed to reach relevant stability of the devices under continuous photo-stress (ISOS-L-2) exceeding 1750h for T_{80} period. The detailed study of surface properties uncovered the interaction of FTPATC with Cs and FA cations, which led to improved thermal stabilization under harsh heating conditions up to 90 °C. We deeply analyzed the specific impact of modifying single interfaces and the synergy of combining approaches with the application of fluorinated SAM. A gathered insights provides a detailed investigation on changes in thin-film/surface properties and physical processes in solar cells.

1.1. Results and discussions

In our work, the surface passivation of charge-transporting interlayers was achieved through the use of FTPATC as a novel SAM. The synthesis of FTPATC is outlined in Fig. 1(a)(b). The initial stage of the synthesis involved an *N*-arylation reaction between 1-bromo-4-fluorobenzene (**1**) and aniline carried out under Buchwald-Hartwig conditions. This resulted in the formation of a difluorine-substituted triphenylamine derivative (**2**), which was obtained in 91 % yield. Subsequently, a non-functional *bis*(4-fluorophenyl)[4-(2-thienyl)phenyl] amine (**5**) was obtained via the bromination reaction of compound **2** with *N*-bromosuccinimide (NBS) in 87 % yield followed by the Suzuki cross-coupling reaction with 4,4,5,5-tetramethyl-2-(2-thienyl)-1,3,2-dioxaborolane (**4**) in 74 % yield. The final stage involved the carboxylation reaction of the *in situ* prepared lithium derivative of the compound **5**, which resulted in the target compound FTPATC being obtained in 70 % yield. Further details and experimental protocols can be found in the ESI (synthetic procedures section). All of the compounds were isolated and characterized by ^{1}H and ^{13}C NMR spectroscopy (see **ESI**, Figs. S1–S8). FTPATC was found to be a crystalline material with a melting temperature of 224 °C and a relatively high decomposition temperature (above 255 °C) (see **ESI,** Fig. S9). Moreover, the absorption maximum of FTPATC in the thin film occurs at 393 nm, which circumvents the «parasitic » light absorption by the HTL in p-i-n device architectures. The HOMO and LUMO energy levels for FTPATC were determined to be −5.42 eV and −2.61 eV, respectively, according to the cyclic voltammetry (CV) technique (see **ESI**, Fig. S10). The estimated HOMO and LUMO energy values allow us to classify FTPATC SAM as a p-type semiconductor material. Whereas, the HOMO and LUMO energy level values taken from the literature for the mixed perovskite $CsFAPbI_{3-x}Cl_x$ we used were given aprox. as −5.5 eV and −3.9 eV, respectively [24,25]. Thus, it can be assumed that FTPATC is quite suitable for the hole transport from the perovskite, whereas in the case of electrons, the charge transport is expected to be hindered due to the mismatch of its LUMO energy level. However, considering the thin thickness of the FTPATC interfacial layers used, a less pronounced decrease in the electron transport can be expected due to the presence of a tunneling effect for the charge transfer. Looking ahead, these conclusions are also traced when analyzing the output characteristics of the devices in which FTPATC was used. The p-side modification resulted in a significant improvement in efficiency compared to the control device, whereas the n-side modification resulted in a slight decrease. However, this deliberate trade-off was aimed primarily at achieving a mutual synergistic effect of device stability increase, which was achieved precisely by using a double side modification.

To evaluate the specific properties of the developed SAM, we analyzed the properties of NiO/FTPATC thin-film structures, multilayer samples with microcrystalline perovskite, and p-i-n solar cells. Briefly, the devices with planar, so-called inverted structures were manufactured with the following architecture (Fig. 1(c)): Glass/ITO (anode)–330 nm/NiO (hole-transport layer, p-type, 20 nm)/SAM interlayer/perovskite absorber (intrinsic, 450 nm)/SAM interlayer/C_{60} (electron

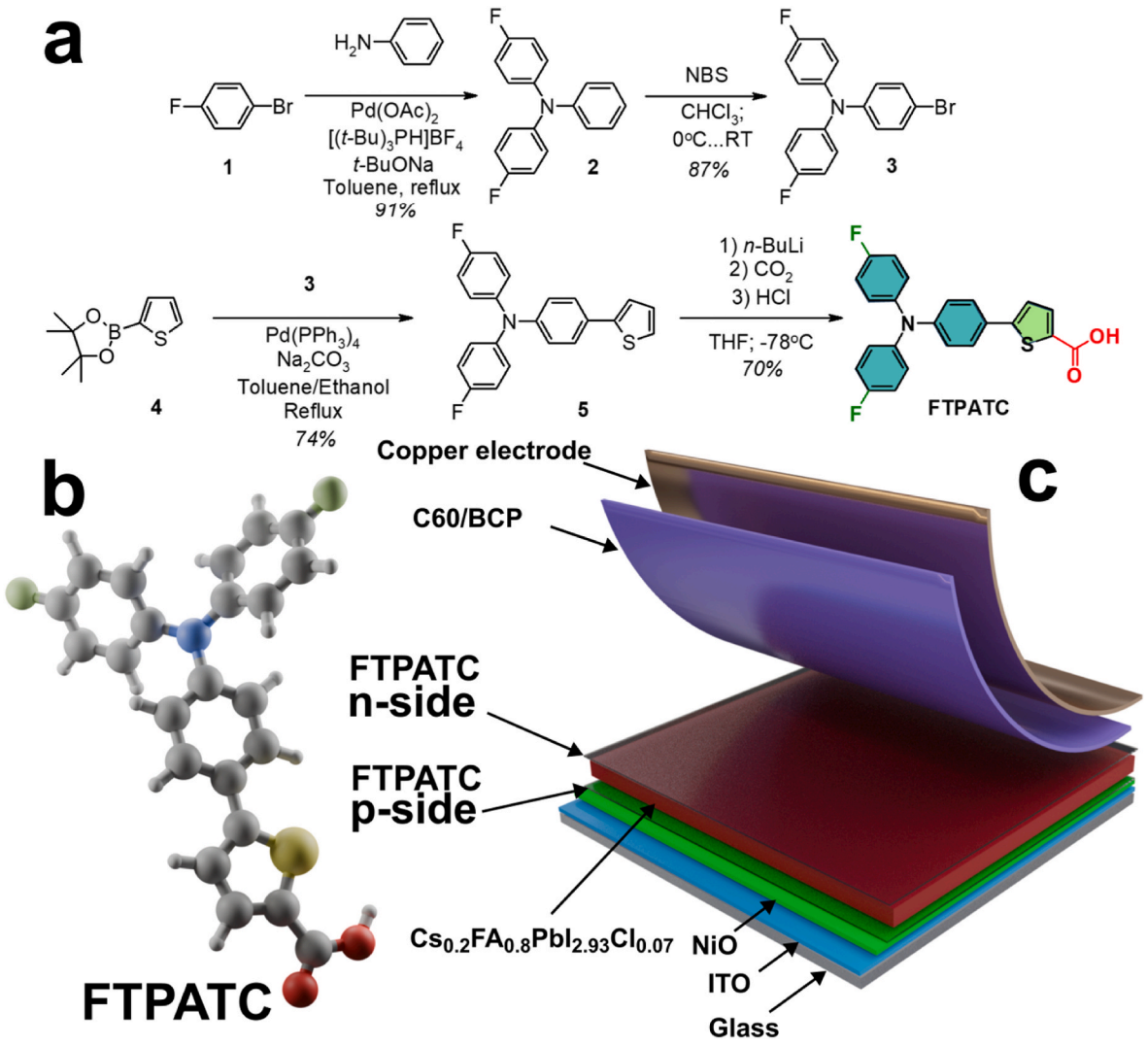

Fig. 1. Synthesis scheme of the compound FTPATC (a); visualization of the FTPATC molecule (b); the device schematics of p-i-n PSCs with integrated SAM interlayers in hole and electron collection interfaces (c).

transport layer, n-type, 40 nm)/bathocuproine (BCP-Ti_3C_2, hole blocking layer, 8 nm)/Bi–Cu (metal cathode, 10/100 nm). The absorber was $Cs_{0.2}FA_{0.8}PbI_{2.93}Cl_{0.07}$ fabricated accord to our previous investigation [26]. The synthesized FTPATC was integrated into NiO/perovskite and perovskite/C_{60} interfaces via solution processing. To simplify sample identification, we used the following names: "control" for bare configurations, "p-side" for configurations with SAM at the HTL/absorber junction, "n-side" for configurations with SAM at the absorber/ETL junction, and "d-side" (double-side) for modifications on both sides of the perovskite thin-film.

To estimate the optical properties of FTPATC integrated to HTLs, we measured the transmittance of thin-films, PL spectra and TRPL dynamics for stacks with perovskite absorber and Tauc plot calculations for extraction of band-gap energy (E_g) (Fig. S11 in electronic supplementary material (**ESI**)). The obtained transmittance plot (Fig. S11(a) in **ESI**) indicates FTPATC parasitic absorption in the short-wavelength region (300–450 nm), corresponding to its wide band-gap. Analysis of the perovskite absorption spectra with Tauc calculation method (Fig. S11 (b), **ESI**) showed that band-gap of perovskite thin-film was ~1.58 eV and hadn't relevant changes for p-side, n-side and d-side configurations. The photoluminescence spectra of perovskite absorber with deposited SAM interlayers presented in Fig. S11(c) (**ESI**). For multilayer structures with the absorber, an increase in photoluminescence intensity was observed for the p-side and d-side configurations compared to the control sample, whereas no changes in signal amplitude were observed for the n-side configuration. Typically, the quenching of the PL signal in multilayer structures with perovskite thin-films is recognized as a signature of photoinduced charge transfer. Such measurements are one of the routine methods for evaluating photo-induced charge transfer in thin-film HP-based structures, although interpreting these results is not always straightforward. As reported in Campanari's work [27], it is not possible to establish a clear relationship between PL quenching and photoelectric performance. We also observed fluctuations in the peak position for the investigated sample configurations within the range of 1.59–1.61 eV, which can be attributed to the reconfiguration of surface trapping states [28]. In our case, the crystallization of perovskite on the FTPATC-modified surface (p-side, d-side) indicates a reduced contribution of non-radiative processes and improved thin-film quality. The obtained trend was supported by TRPL data (Fig. S11(d) and **Table S1** in **ESI**). While, the extracted total charge carrier lifetime was almost equal for control and n-side samples (~42 ns), the p-side and d-side showed an increase up to ~50 ns, obviously originated from the presence of FTPATC at hole collection interface. Increased carrier lifetime in multilayer samples with HP thin-films is generally indicative of reduced recombination rates, so the charge carriers can exist for longer periods before SRH recombination [29,30].

The specific feature of the SAM for interface integration in PCSs is tuning of the surface wettability. Incorporation of SAM on HTL could enhance hydrophobicity and impacts on crystallization dynamics of the perovskite thin-films. The measurements of the wetting angle (**WA**) on bare and modified NiO surfaces (Fig. S12, **ESI**) revealed increase of from 26° to 74°. The investigation surface morphology for the control and p-side multilayer stacks (Fig. S13, **ESI**) exhibited almost equal average grain size ~120 nm.

Despite the absence of notable changes in the morphology of perovskite layers with SAM, the analysis of structural properties could give an insight for differences in lattice parameters, phase composition and possible strain-effects. X-ray qualitative phase analysis was conducted on control, p-side, n-side, and d-side samples, as depicted in Fig. S14 (**ESI**). The predominant phase observed in all samples was the *P4/mbm* tetragonal phase of β-$CsFAPbI_3$, characterized by peaks at 14.08°, 19.96°, 22.33°, 24.50°, 26.51°, 28.35°, and 31.80°. No additional phases were detected. The introduction of FTPATC notably influenced the peak positions of the perovskite phase (Fig. 2(a)). Lattice parameters were calculated using the Rietveld method and are presented in **Table S2** (**ESI**). For the p-side sample, the parameter "a" changed from 8.904 Å in the control sample to 8.923 Å upon FTPATC application. Covering the perovskite with FTPATC resulted in compression of the "c" parameter from 6.314 Å in the control sample to 6.302 Å in both the n-side and d-side samples. In contrast to n-side sample, the d-side had lattice parameters of a = 8.907 Å and c = 6.302 Å. This displays a distinct decrease in crystal unit cell size, leading to the initiation of compressive strain in the perovskite film. As reported [31], compressive strain enhances phase stability of the perovskite film associated with ion migration.

To reveal the features of the interlayer interaction for perovskite/FTPATC, we conducted XPS analysis. The survey spectrum is shown in Fig. S15 (**ESI**), with changes in elemental composition detailed in **Table S2** (**ESI**). The high-resolution F1s spectrum (Fig. 2(b)) confirms the presence of fluorine on the back surface of the absorber (electron collection side) as well as at the buried interface with HTL (p-side bottom). Comparing the bare absorber with perovskite/FTPATC (n-side), we observed a 0.15 eV shift in the Cs3d5/2 maximum (Fig. 2(c)). Fitting the components of the corresponding Pb4f peaks (Fig. 2(d)) indicated area changes in line intensities at 138.9 eV. Notably, for the outer shell electrons of Pb5d5/2 (Fig. 2(e)), a shift to lower binding energies (increased kinetic energy) was observed for the n-side configuration. This results in total shift of the maxima valence bend towards Fermi level from 1.55 eV (control) to 1.26 eV (n-side) as shown in Fig. S16 (**ESI**). N1s spectra presented in Fig. S17 (**ESI**). So, the resulting changes of the energy level position for perovskite/FTPATC interface reached ~0.3 eV compared to Control sample.

In order to elucidate potential chemical interactions for FTPATC with organic cation of the perovskite molecule (formamidinium), the set of liquid-state proton nuclear magnetic resonance (^{1}H NMR) studies was conducted in DMSO solution (Fig. 2(f)). The NMR data indicated the presence of the broad peak, attributed to four equal $-NH_2$ protons, at δ 8.75 ppm, while the formyl singlet proton peak was observed at δ 7.84 ppm, for pure formamidinium iodide (FAI), which in accordance with the literature data (full spectra, in Fig. S18, **ESI**). The followed addition of FTPATC, the weak carboxylic acid, resulted in a significant change in the spectrum (1:1 M ratio). The equivalence of the $-NH_2$ protons was no longer observed, and the presence of two signals at δ 8.99 and δ 8.64 ppm was noted, while the formyl proton located at δ 7.84 ppm was recorded as a triplet of triplets. The similar pattern, previously observed in the literature when adding molecular iodine (I_2) to FAI in DMSO solution, indicated the formation of strong hydrogen bonds between amino-protons and the triiodide anion (I_3^-) via η^3-allylic complexes shaping, which is not observed for the iodide anion (I^-) [32]. Furthermore, the formamidinium triiodide single crystal was isolated and characterized in its individual state [33]. Based on the aforementioned considerations, it can be proposed that a comparable observation was likely to occur for the FAI and FTPATC interaction. The presence of hydrogen bonds ensures the binding of FTPATC on the perovskite surface through the chemical interactions with the organic cation, which, in some studies, is considered as a proxy for better passivation [34]. Slight changes in the cesium peak position, along with NMR data, indicate that FTPATC forms chemical bonds with the A-site cations of the perovskite molecule, specifically Cs and FA. We should note that XPS exhibited considerable changes only in outer shell electrons energy, which could be originated from the locally enhanced electric field on the surface induced by formation of the dipole [35].

To explore the possible changes in optoelectronic properties of the modified thin-films, we used KPFM (Kelvin probe force microscope) technique. Analyzing the surface potential of multilayer HTLs with a perovskite layer is not trivial. These studies require consideration of the

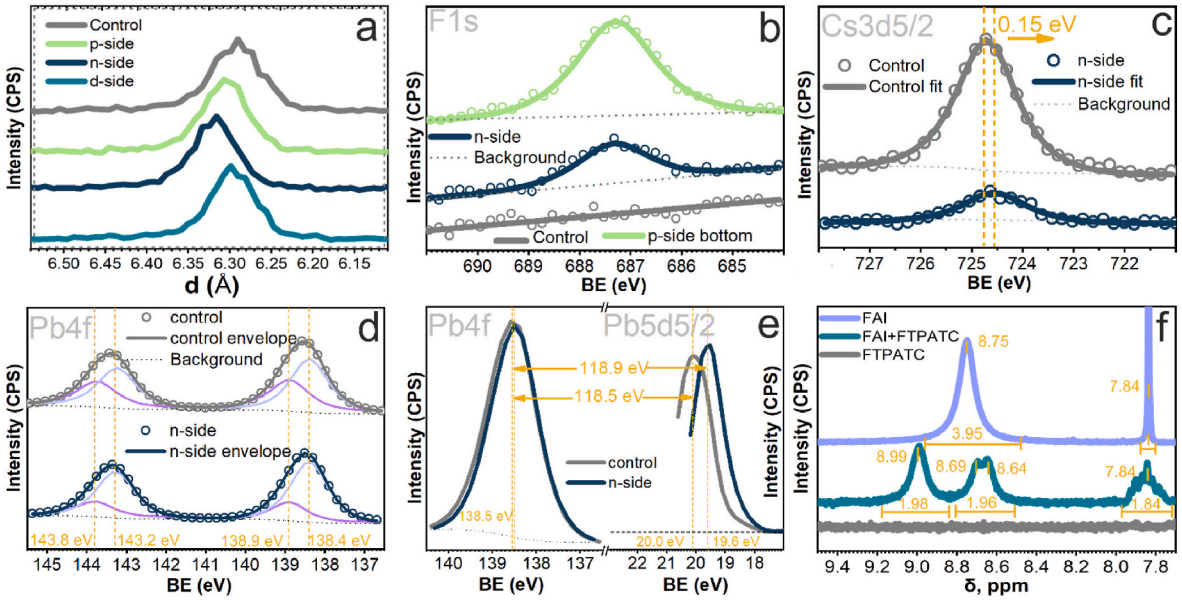

Fig. 2. XRD patterns of perovskite films with FTPATC in different interfaces (a); high resolution XPS spectra of F1s (b); Cs3d5/2 (c); Pb4f (d); Pb5d5/2 (e) for perovskite with and w/o FTPATC and ^{1}H HMR spectra of FAI, FTPATC and their blend in *d*-DMSO solution (f).

properties of individual thin-films as well as the buried interface of the absorber, where the surface state plays a crucial role in photo-carrier charge transport. We performed the mapping of the surface potential measurements with calculations of the work-function values for charge transporting layers stacks and de-laminated perovskite absorber with SAM interlayer (Fig. 3 (a) and Fig. S19 in **ESI**). The calculated mean W_f for the surfaces of bare NiO and FTPATC HTL were close, with values of 4.69 and 4.67 eV, respectively. The observed KPFM data showed that the FTPATC interlayer reduces the energy level offset (ΔE) between NiO and the absorber from 0.46 to 0.08 eV. This could potentially reduce the impact of hole accumulation at the interface, reduce the dynamics of non-radiative recombination processes, and increase charge-carrier extraction efficiency. Analysis of the top (electron collection) side of the absorber showed that bare perovskite film has W_f of 4.48 eV, while for n-side configuration we observed a shift to 4.57 eV. Hypothetically, this could affect to energy level alignment with C_{60} ETL which has the position of lowest unoccupied molecular orbit at ~4.2 eV [36]. However, the complex impact of surface modification on quasi-Fermi level splitting under light exposure requires analysis of PSC output.

Further, we made the analysis of interface passivation with FTPATC on the output of the p-i-n devices. To investigate the photoelectric performance of the fabricated PSCs, we used standard illumination conditions (AM 1.5 G spectra, 100 mW/cm^2, 25 °C) employing AAA Xe solar simulator. The box-charts with statistical distribution of output parameters (open circuit voltage- V_{oc}, chort-circuit current density - J_{sc}, filling factor–FF, power conversion efficiency - PCE) extracted from the volt-ampere (**IV**) curves presented in Fig. S20 (**ESI**). The performance of the champion devices is shown on Fig. 4(a). All IV characterization was conducted in the ambient conditions for the encapsulated devices. The best (average) PCE of control PCSs reached the values of 20.2 % (18.9 %). The devices of p- and d-side configurations showed a relevant increase in PCE up to 22.2 % (19.4 %) and 21.3 % (19.6 %), respectively. In contrast, the n-side devices exhibited a slight reduction in PCE with values of 19.9 % (18.3 %). Primarily, the changes in PCE were driven by V_{oc} and $J_{SC,}$ while the average/best FF values for all device configurations fluctuated in the narrow range of 78–79 %. In solar cells, the V_{oc} value related to quasi-Fermi level (**QFL**) splitting, which occurs in the perovskite absorber during photo-injection. Theoretically, V_{oc} and QFLS values should be very close, but experimental results typically demonstrates that V_{oc} is much lower. The large mismatch between QFL and open-circuit voltage in the devices originates from the energy level offset for absorber and charge transporting layers, combined with the processes of the interfacial recombination. This could cause unfavorable bending of the energy levels, leading to a reduction in V_{oc} and affecting charge carrier transport efficiency. Our results highlight that interface modification with FTPATC has a significant impact on V_{oc} changes. The best (average) V_{oc} values for the control devices were 1.08 V (1.07 V). P-side PCSs increased to 1.13 V (1.10 V), while d-side devices exhibited the strongest gain, achieving 1.14 V (1.13 V). Interestingly, for the n-side configuration, we observed a decrease in V_{oc} to 1.06 V (1.03 V), which is lower than the control. Notably, d-side devices, which also have FTPATC on the electron collection side, didn't show this trend. This indicates that reconfiguring energy level alignment and FLP in the absorber should be combined to achieve an optimal W_f shift. The changes in J_{sc} for PCSs with SAM were less dramatic, but statistical analysis clearly showed the effect of interface engineering. The J_{sc} for control PSCs was 23.7 mA/cm^2 (22.6 mA/cm^2). For the p-side configuration, the mean values were similar −22.7 mA/cm^2, although the champion value reached 24.6 mA/cm^2. We observed a statistically proved increase in J_{sc} for the n-side configurations at 23.6 mA/cm^2 (23.1 mA/cm^2), as well as for the d-side, which had the highest J_{sc} values at 24.2 mA/cm^2 (23.6 mA/cm^2). The observed results demonstrate that double-sided interface engineering with SAM has a complex impact, with specific effects on both hole and electron-transport interfaces.

Interface modification with FTPATC had a notable effect on device J_{sc} confirmed by external quantum efficiency spectra presented on Fig. 4 (b). J_{sc} extraction via EQE spectrum integration (AM 1.5 G conditions) demonstrated an increase in photocurrent from 20.8 mA/cm^2 for the control device to approximately 22 mA/cm^2 for PSCs with a SAM interlayer. We observed enhanced photoelectric conversion across the entire absorption spectrum of the $CsFAPbI_3$ absorber. Configurations with FTPATC at the HTL interface (p-side, d-side) exhibited a characteristic gain in the short wavelength region of 380–420 nm. Photons with higher energy are more efficiently absorbed in the near-surface region of solar cells, indicating improved hole collection efficiency and the absence of parasitic absorption by the FTPATC interlayer.

The stabilization of the output performance was estimated with maximum power point ($\mathbf{P_{max}}$) tracking (MPPT) of PSCs (Fig. 4(c)) under standard conditions of illumination. Control devices showed absence of the light-soaking effects on P_{max} for 500 s. We found that p- and n-side configurations have the opposite trends for the stabilization. P-side devices showed slight increase in P_{max} before saturation (+~1.2 %), while n-side PCS have a reduction in ~2 %. This displays different nature of the traps-filling process under photo-injection, which is typically associated with light-soaking/accumulation effects. Finally, the d-side PSC also had the negligible fluctuation of P_{max}, which could be originated from complex impact of energy level alignment.

The transport properties of PSCs were evaluated through an analysis of the dark JV curves (Fig. 4(d)). The devices demonstrated relevant diode behavior with strong electrical rectification. The use of SAM effectively reduced the leakage current ($\mathbf{J_L}$), correlating with the type of interface modification. For the control device, the J_L value (−0.2 V bias) was 10^{-4} A/cm^2. Incorporating FTPATC in single-side configurations reduced this value by an order of magnitude, while for d-side PSCs, J_L reached 10^{-6} A/cm^2. The shunt resistance ($\mathbf{R_{sh}}$) calculation showed a significant increase, from 3.6 kOhm·cm^2 for the control to 446 kOhm·cm^2 for the d-side. The dark volt-ampere characteristic of the solar cell can be divided into four main sections: shunt current (I), recombination current (II), diffusion current (III), and contact resistance (IV). For comprehensive analysis of the charge transport in control and target PSCs, we performed a fitting of dark JVs using 2-diode model (Fig. S21, **equations S1-S8**, see **ESI** for the details) and extracted the

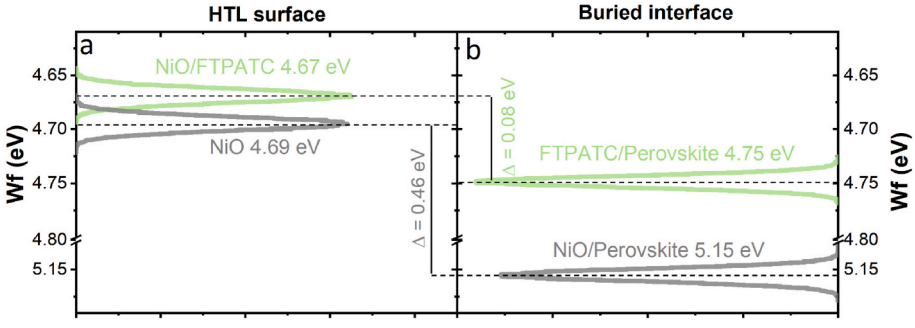

Fig. 3. The W_f values measured for the HTL surface (a) and buried interfaces of the HTL/absorber (b).

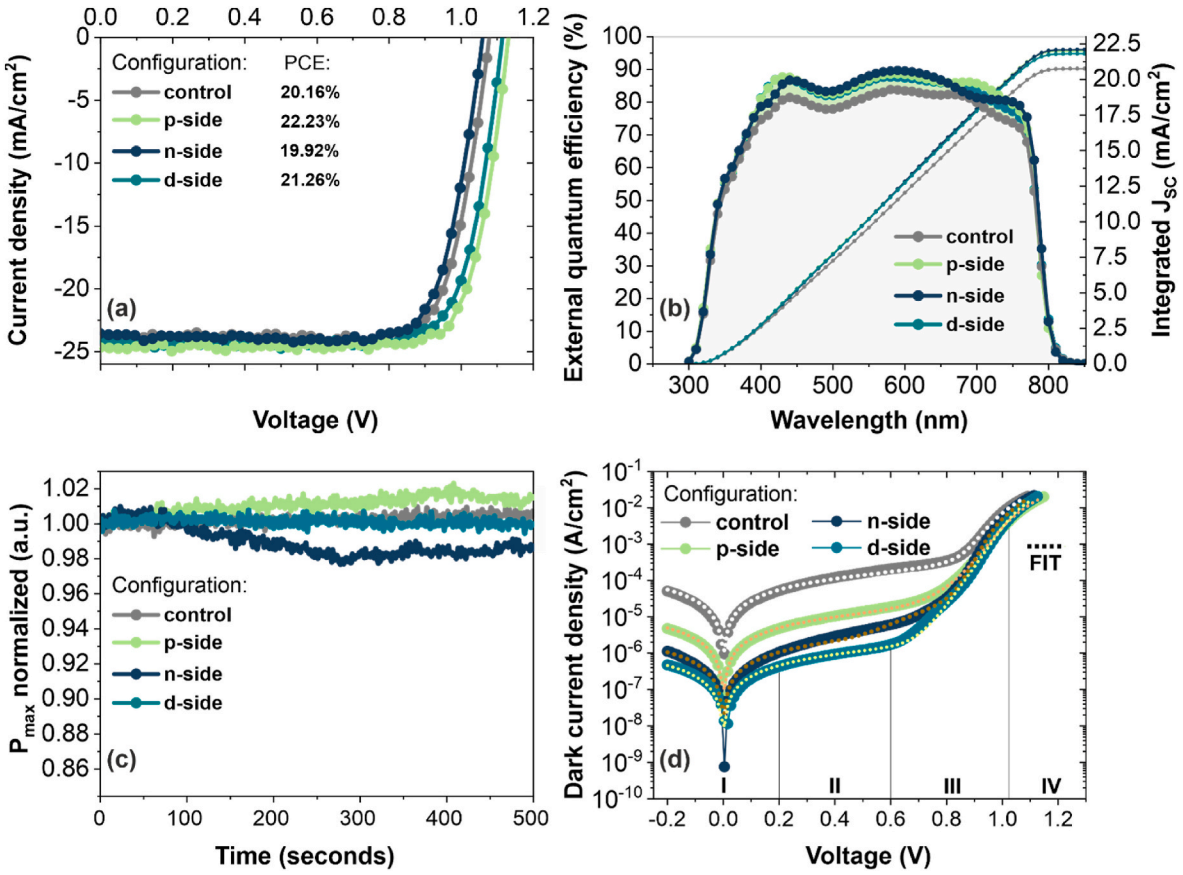

Fig. 4. The JV curves for the PSCs with champion performance (a); external quantum efficiency spectra for the representative PCSs (b); initial stabilization of maximum power under standard illumination conditions (c); dark JV curves with fitting using 2-diode model (d).

specific parameters: non-ideality factor (**n**); dark saturation currents ($\mathbf{J_0}$). The physical meaning of the non-ideality factor is closely related to the dominant recombination processes occurring within the photodiode. For the well-established diode architectures (like Si or $A_{III}B_V$ devices), the n values typically are in the range between 1 and 2. When n is close to 1, it indicates that the dominant recombination process occurs in the bulk (neutral) regions of the photodiode (recombination goes primarily due to band-to-band transitions). The increase of n value up to 2 suggests the shift of the dominant recombination process to interfaces involving trap states (so-called Shockley-Read-Hall (SRH) recombination). Due to the presence of two hetero junctions, applying standard models to HP-based p-i-n diode structures is complex. Therefore, the recombination processes in PCSs are not accurately described by an n range of 1–2, and corresponding equivalent electrical circuits require modifications. In this work, we used a 2-diode model with series-connected diodes, where the total n for the device was the sum of the individual values. The extracted n (**Table 1**) showed the highest value for the control PSC (2.31), while device with single-side modifications (p- and n-configurations) had reduced and almost equal non-ideality factors ~2.14. D-side PSC demonstrated the synergetic effect of SAM integration, reaching the n = 1.58. This trend reveals the beneficial role of FTPATC in the suppression of unfavorable trapping processes at the interfaces. The decrease in J_0 for the devices with interface modification (see Table 1) support the observed findings. Calculated series resistance values ($\mathbf{R_s}$) showed negligible changes with fluctuations of the values in the range of 2–3 Ohm*cm^2.

To further analyze charge carrier extraction properties of PSCs, we conducted transient photocurrent (**TPC**) measurements, presented in Fig. 5(a)(b). When the solar cell is irradiated with a short light pulse, photo-generated charge carriers (photocurrent) are collected at the electrodes. Using a square waveform of the light signal, the device operates in **ON** and **OFF** modes, with the corresponding output at signal saturation. Analyzing the dynamics of the signal rise and decay, as well as the shape of the photo-response, allows to evaluate the contribution of recombination processes and charge accumulation impact. The rising and falling times ($\mathbf{t_r}$ and $\mathbf{t_f}$) were calculated from the change in photocurrent amplitude from 10 % to 90 % respectively. For the control sample, the t_r was 10.5 μs, while all configurations with the FTPATC interlayer demonstrated more rapid signal dynamics. Notably, single-side modifications of the interfaces showed variations in the TPC time profile. P-side devices exhibited a t_r of 8.7 μs, and the n-side showed the lowest t_r of 5.5 μs. The d-side configuration showed an averaged value of t_r of 7.4 μs. Analyzing the t_f values showed a similar trend in TPC improvements. It is also notable that the control device clearly exhibited an

Table 1
The extracted parameters for the fitting of dark JV curves using 2-diode model.

Device configuration	n_1	n_2	n (n_1+n_2)	J_{01}, A*cm^{-2}	J_{02}, A*cm^{-2}	R_s, ohm*cm^2	R_{sh}, ohm*cm^2
Control	1.175	1.131	2.306	2.51E-13	1.46E-6	2.46	3.61E+03
p-side	1.121	1.022	2.143	1.95E-14	4.99E-7	3.19	4.07E+04
n-side	1.082	1.066	2.148	2.26E-14	5.83E-7	2.57	1.95E+05
d-side	0.874	0.704	1.578	1.15E-14	7.95E-9	3.21	4.37E+05

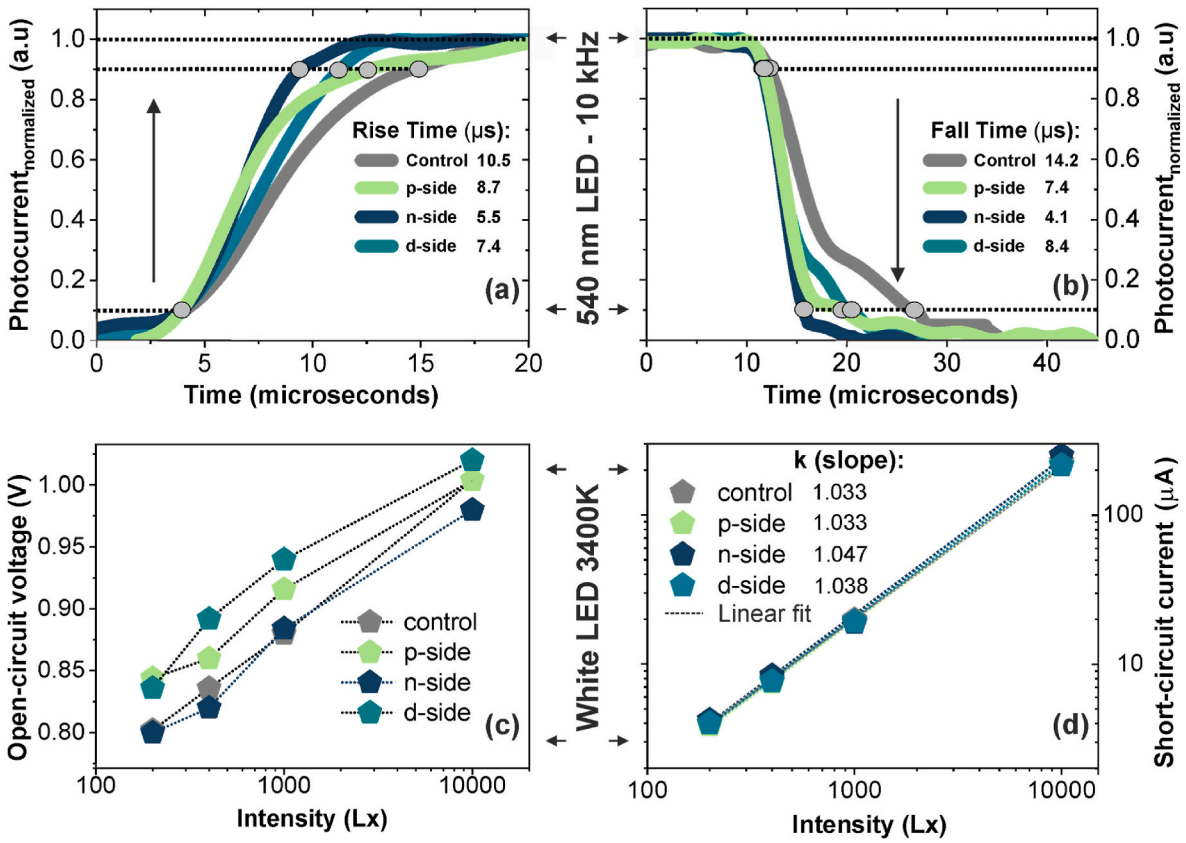

Fig. 5. The transient photo-current measurements in RISE mode (a); transient photo-current measurements in FALL mode (b); V_{oc} vs. light intensity dependence for low-light illumination (c); J_{sc} vs. light intensity dependence for low-light illumination.

additional slow component in the decay signal. This feature in the transient response of HP-based optoelectronic devices is typically caused by ion migration at the interfaces (uncompensated organic cations, etc. [37]), strain in the crystal structure and trapping processes [38]. The increase in t_r/t_f of the transient response can be described by capacitive effects using various models [39]. The reduction in transient time for the devices with FTPATC clearly indicates enhanced charge carrier extraction efficiency, with t_r/t_f reductions ranging from 20 % to over 100 % compared to the control PCSs. Integrating SAM into the electron-transport junction resulted in the maximum improvement of photo-response dynamics and leveling of the signal's capacitive components.

We performed intensity-dependent performance measurements to analyze the difference photo-response (Fig. 5(c)(d)). PSCs were illuminated with white LED sources at intensity levels ($\mathbf{I_0}$) from 200 to 10,000 Lux, corresponding to indoor low-light conditions. Under conditions of low concentrations of photo-injected photo-carriers and reduced photocurrent, the contribution of recombination processes and transport efficiency allow for a more precise identification of the specific effects induced by interface modifications in PSCs. The V_{oc} values showed a logarithmic dependence ($V_{oc} \propto$ ln (photocurrent/dark saturation current) [40], whereas the J_{sc} trends were linear (photocurrent $\propto$ carrier generation rate) [40]. Generally, V_{oc} vs. I_0 exhibited changes similar to the mean values measured under standard conditions (AM 1.5 G). At 10^4 Lux, d-side devices had a V_{oc} of 0.02 V higher compared to control and p-side device. However, the relative difference between control and d-side devices increased to 0.05 V at light intensities of 10^2 -10^3 Lx. This points to an increased losses of charge carrier splitting in mentioned low-light intensity range, due to the complex contribution of shunts and trapping processes. In the analysis of J_{sc} vs. I_0, we observed a different behavior for PSCs' performance. Calculation of the slope coefficient (**k**) of the linear dependence indicated that the n-side and d-side configurations were characterized by an increased steepness, whereas the p-side and control configurations had equal values. The fill factor also revealed differences in intensity-dependent photo-response (Fig. S22, ESI). The n-side and d-side configurations exhibited reduced FF losses, the control and p-side in contrast, revealed more sensitive behavior at I_0 ~10^2–10^3 Lx. The observed IV pattern under low-light illumination indicates improved electron collection efficiency with FTPATC integration at the absorber/C_{60} contact, and clearly highlights the critical impact of diode properties.

To reveal the numerical parameters of the mobile ion-species in the fabricated PSCs, we used Admittance Spectroscopy (**AS**) measurements. For the control device (Fig. 23(a) in **ESI**), AS spectroscopy results indicate the presence of two mobile ions, one at high temperature (E_A = 0.58 eV, D_0 = 163.4 cm^2/s) and another at low temperature (E_A = 0.72 eV, $D_0 = 1.66 \times 10^{11}$ cm^2/s). In contrast, samples with SAM modifications exhibited only the high-temperature ion (Fig. S23 (b - d)). While the concentration remains within one order of magnitude for p-, n-, and d-side samples (~10^{14} cm^{-3}), the p- and d-side samples show a lower concentration of the 0.58 eV ions (Fig. S24, **ESI**).

In parallel, we investigated the stability of the output performance under continuous photo – and thermal stress. Stability tests were conducted on encapsulated devices in ambient conditions with humidity levels not exceeding 60 % RH. The conditions of the long-term light-soaking (**LS**, Fig. 6) followed to the ISOS-L-2 protocol [41] (open-circuit mode of operation, 3400K LED illumination, 63.5 ± 1.5 °C). The normalized data of LS performance for PSCs presented in Fig. S25 (**ESI**). All device configuration demonstrated relevant photo-stability over 1600h before T_{80} conditions. Notably, that after soft-heating conditions, PSCs showed an initial drop of the performance that followed by an increase with saturation. Such effects results from the complex processes of the temperature-related changes in charge-splitting and its collection, as well as rearrangement of the traps. Accord to the notes of the ISOS

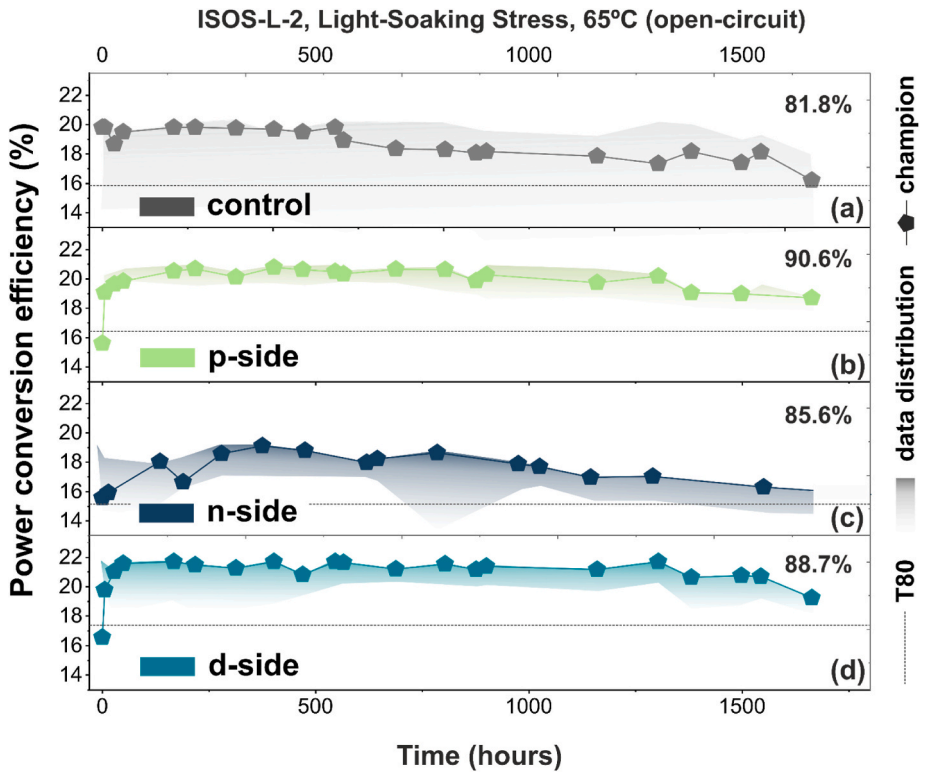

Fig. 6. Stability performance of PSCs under continuous Light-Soaking Stress and soft heating (63.5 ± 1.5 °C) for various configurations.

protocol, for the devices with a positive trend in PCE, T_{80} period should be estimated for time at which the efficiency has dropped to 80 % of the maxim value, with the complete time from 0 h to this point quoted as the T_{80}. After 1680h of LS, the champion control device reached the level of 81.8 %, which was the lowest compared to other configurations. Moreover, statistical distribution of the LS stability data showed that other devices of the batch (control configuration) have fluctuations in the performance with T_{80} even lower 1000h. P-, n- and d-side devices exhibited slight enhancement of the stability with 90.6, 85.6 and 88.7 % of the performance after 1680h supported by narrow data distribution.

We also conducted studies under harsh heating conditions up to 90 °C (ISOS-D-2). The performance loss rate for PSCs was more rapid

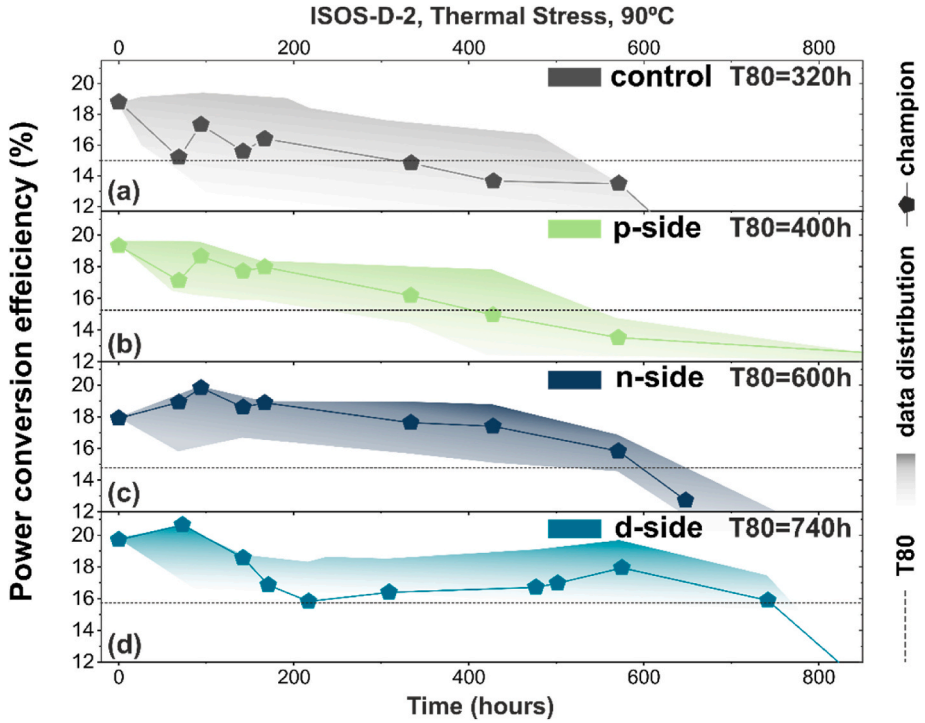

Fig. 7. Stability performance of PSCs under continuous harsh-heating conditions (90 °C) for various device configurations.

under enhanced heating stress compared to LS, revealing a thermal stability threshold between 60 and 90 °C (Fig. 7). Control PSCs achieved T_{80} after 320 h, after which their power fluctuated between 80 % and 90 %. The P-side configuration did not significantly differ from the control sample, with T_{80} at 390 h. PSCs with FTPATC on the ETL side (n- and d-configurations) showed improved thermal stability up to 600–740 h, which significantly differed for the trends observed for LS conditions. The normalized data of thermal stability performance for PSCs presented in Fig. S26 (**ESI**). We found that modification of p-side interface almost doesn't impact the thermal stability at the elevated temperatures (90 °C), while n-side modification offers a notable gain in suppression of the power losses. This indicates that corrosion processes are strongly accelerated on the back (electron-collection) side of the p-i-n solar cells harsh heating conditions. Clearly, elevated temperatures accelerate multiple degradation factors in PSCs. In context of the interface stability topic, the initial corrosion processes related the defect-ion migration, as well as release of the gaseous decomposition products from the perovskite absorber [42]. At the elevated temperatures (90–95 °C), the FA-based HPs could undergo the irreversible decomposition [43] with formation of NH_3, $C_3H_3N_3$, HI, I_2 and PbI_2. The presence of A-site defects in HP structure (uncompensated ions, vacancies) promotes distortions in lattice environment, and changes in stoichiometry conditions (iodine-rich, etc.), which, in turn, could induce unfavorable phase transition. Moreover, the migration of the organic A-site ions and iodine-containing products towards the back electrodes under electric field impacts to the degradation of metal cathodes [44]. The observed results of PSC stabilization with FTPATC indicate a beneficial impact when integrating SAM on the electron collection side. FTPATC interacts with the FA-cation on the surface of the absorber, preventing it from transitioning to a free gaseous state under heating conditions. Furthermore, since FTPATC contains an electron-deficient carboxyl group (-COOH), there are several possibilities for passivation of defects in perovskite by FTPATC, as reported in the literature [45]. These mechanisms include Coulomb interactions between undercoordinated metal ions and the carboxyl group, as well as the formation of hydrogen bonds between FA and COOH fragments. These strong interactions prevent thermal degradation of the device, thus increasing its stability under thermal stress. Moreover, it is well-established that organic fluorine-containing additives, due to their hydrophobic nature, are more effective at protecting perovskite materials from moisture [16]. Additionally, dipole formation at the interface with FTPATC can screen ionic defects during migration in the electric field. Employing double-sided passivation for PSCs combines the advantages of p-side energy level alignment, reduction of lattice stress, and suppression of corrosion processes on the back surface. The developed approach is particularly important for up-scaling issues. Typical exploitation temperature of solar panels in ambient conditions reaches the range of 85–100 °C. Therefore, the accelerated corrosion processes at the interfaces should be mitigated not only at standard (25 °C) or soft regimes (65 °C), but also for harsh heating. Despite non-optimal energy level alignment with FTPATC at ETL interface, the reduction in charge transport efficiency is not critical. The ultrathin SAM layer could potentially allow for charge transport via a tunneling mechanism. The key advantage of FTPATC is its enhanced thermal stability at temperatures up to 90 °C, as demonstrated in both n-side and d-side configurations.

Comparing the FTPATC molecule with standard SAM materials may offer deeper insights into the stabilization specifics of our single and double-side passivation approach. To facilitate a direct comparison with FTPATC, we employed the widely-used 2PACz molecule ([2-(9H-carbazol-9-yl)ethyl]phosphonic acid). Optimizing the deposition process for each SAM requires adjustments to fabrication methods, solution concentrations, and post-treatment. In this study, we conducted an initial experiment where both p-side and n-side modifications with 2PACz were fabricated using an isopropanol (IPA) solution (see ESI for details). For the n-side configuration, solvent compatibility with perovskite films is crucial, as IPA solutions can affect the organic cation in the perovskite molecule. The JV curves and box-charts displaying the statistical distribution of output performance for the batch are presented in Fig. S27,**28** in **ESI**. The incorporation of 2PACz led to an increase in V_{oc} to values exceeding ~1.1 V, validating the improved in energy level alignment at the HTL/perovskite interface.

Stability measurements under heat stress are shown in Fig. S29 (**ESI**). The control devices exhibited similar performance to control devices used for the FTPATC batch, with a T_{80} ~300 h. In contrast, devices with 2PACz applied on the p-side exhibited a reduced T80 of 150 h, which may be attributable to the need for optimization of the interlayer thickness. The increased contact resistance observed in the 2PACz p-side devices suggests an accumulation effect at the interface. In devices with 2PACz on the ETL side (n-side, d-side), corrosion processes occurred rapidly, within 24 h.

The decomposition temperature of 2PACz is 214 °C [46], which is lower than that of FTPATC (254 °C), but it ensures intrinsic stability under thermal-stress at 90 °C. For these samples, we visually identified a characteristic perovskite color change, indicating complex degradation and possibly a phase transition (Fig. S30 in **ESI**). This observation led to the conclusion that 2PACz is not an effective agent for passivating defects from the ETL side, as it accelerates corrosion processes. First, using a 2PACz solution in IPA is not fully compatible with ETL interface modification. IPA is known to interact with organic cations within the perovskite structure and uncompensated Pb ions [47]. As a result, 2PACz deposition in IPA may disrupt the surface stoichiometry of $CsFAPbI_3$, potentially inducing phase segregation or decomposition.

Furthermore, the n-side modification difference may be due to the electronic nature the SAMs being compared. The FTPATC SAM featured by an obvious push-pull molecule structure, which can stabilize the electron-rich triphenylamine fragment through electron/charge delocalization, whereas 2PACz is represented by an electron-rich carbazole fragment not conjugated with a phosphorus group [48]. Taking into account the above, we can assume that not only the absence of stabilization, but also more accelerated degradation in the case of n-side modification for devices using the 2PACz-SAM can be caused either by the space charge effects or by possible chemical/electrochemical reactions, or interlayer diffusion processes. The first assumption follows from the higher LUMO energy values for 2PACz compared to FTPATC. To address the second assumption, we performed CV measurements for the commercial 2PACz we used, comparing the data obtained with previously reported for FTPATC (Fig. S31, **ESI**). 2PACz has by a deeper-lying HOMO energy level compared to FTPATC, which follows from the lower oxidation potential for it (+1.18 V vs +1.02 V, respectively), whereas the experimentally HOMO energy value for it was estimated as −5.58 eV, which in an agreement with previously published data [49]. Noted the irreversible nature of the electrochemical oxidation process for 2PACz, whereas FTPATC was oxidized quasi-reversibly, which makes potentially more stable interface from the p-side. By analyzing the electrochemical reduction for 2PACz, we observed the irreversible process occurring at reduction potential values of about −0.84 V. Taking into account both the band gap and optical properties for 2PACz [50], this reduction process cannot be associated with the electron affinity and, as a consequence, cannot characterize the LUMO level energy for it. However, the fact of the presence and registration of this reduction process, caused by either the possible presence of impurities in commercial 2PACz sample, or the possible process of its electrochemical dissociation, we can indirectly interpret as a lower electrochemical stability of 2PACz, compared to FTPATC.

It can be stated that the application of SAM for double-side passivation is not a universal approach for such materials. Our results demonstrate that the use of FTPATC has synergetic stabilization effects when integrating SAMs on the ETL side in p-i-n structured PSCs. To further improve the output performance of double-side passivated devices, it will be essential to enhance the energy level alignment at the ETL interface.

We compared our data with state-of-the-art SAM applications for

PSCs (**Table S3** in **ESI**). Achieved PCE of 21–22 % is relevantly comparable to the best PCE values for p-i-n devices [51]. Most reports evaluate device stability without considering harsh thermal conditions. Our research underscores the importance of n-side interface modifications with SAM, which enhance stability at elevated temperatures [48]. Future performance optimization should focus on energy level alignment with ETL. The stability data are superior to alternative double-sided passivation approaches [52] or comparable to methods employing more advanced interface engineering [53].

2. Conclusions

In conclusion, our complex investigation introduces an effective approach for double side interface modification in high-performing p-i-n PSCs. The incorporation of FTPATC to charge-collection junctions reduced the potential barriers and improved energy level alignment with perovskite absorber. This promoted suppression of the recombination dynamics at the hole/electron collection interfaces in the devices and enhanced diode properties. We found that modification of p- and n-type collection junctions has different specifics which impacts to photoelectric output and long-term stability. While p-side integration of FTPATC reduced the strain in the lattice of the perovskite layer, the n-side configuration was characterized by chemical interaction via bonding with A-site cations, which stabilized the interfaces. With this, the double-side passivation strategy with FTPATC has a synergetic effect: p-side modification gains the PCE up to 22.2 %, the incorporation of FTPATC to electron-transport boosts the stability of the devices under harsh conditions at the elevated temperatures (90 °C). Comparing our results with the benchmark material 2PACz highlighted a critical specificity in ETL interface modification. The standard SAM containing carbazole fragments and a phosphorus group used for n-side modification led to accelerated degradation under thermal stress. By contrast, FTPATC is more universal and provides enhanced interface stabilization due to its electron-rich triphenylamine fragment and peripheral fluorine atoms. This result offers an important basis for further optimizing SAM properties for n-side passivation, particularly for achieving better energy level alignment. This research offers an important insight into co-modification strategy of the front and back interfaces of the perovskite absorber for balanced optimization of efficiency and stability. Solution-processing with FTPATC could be easily up-scaled for large-area perovskite solar modules in further development.

CRediT authorship contribution statement

Ekaterina A. Ilicheva: Writing – original draft, Methodology, Formal analysis, Data curation. **Polina K. Sukhorukova:** Writing – original draft, Resources, Investigation, Formal analysis, Data curation. **Lev O. Luchnikov:** Writing – original draft, Methodology, Investigation, Formal analysis, Data curation. **Dmitry O. Balakirev:** Resources, Methodology, Investigation, Data curation. **Nikita S. Saratovsky:** Investigation, Formal analysis. **Andrei P. Morozov:** Methodology, Data curation. **Pavel A. Gostishchev:** Methodology, Formal analysis. **Sergey Yu. Yurchuk:** Methodology, Formal analysis. **Anton A. Vasilev:** Methodology, Formal analysis. **Sergey S. Kozlov:** Methodology, Formal analysis. **Sergey I. Didenko:** Methodology, Data curation. **Svetlana M. Peregudova:** Investigation. **Dmitry S. Muratov:** Visualization. **Yuriy N. Luponosov:** Writing – original draft, Supervision, Methodology, Funding acquisition, Formal analysis, Data curation, Conceptualization. **Danila S. Saranin:** Writing – original draft, Supervision, Project administration, Methodology, Investigation, Funding acquisition, Formal analysis, Data curation, Conceptualization.

Declaration of competing interest

The authors declare that they have no known competing financial interests or personal relationships that could have appeared to influence the work reported in this paper.

Acknowledgements

The work was supported by the Russian Science Foundation (project № 22-19-00812) - https://rscf.ru/project/22-19-00812/and conducted at NUST MISIS. NMR spectra were recorded using the equipment of the Collaborative Access Center 'Center for Polymer Research' of ISPM RAS with support from the Ministry of Science and Higher Education of the Russian Federation (topic FFSM-2024-0003).

Appendix A. Supplementary data

Supplementary data to this article can be found online at https://doi.org/10.1016/j.mtener.2024.101741.

Data availability

Data will be made available on request.

References

[1] N. Yaghoobi Nia, D. Saranin, A.L. Palma, A. Di Carlo, Perovskite solar cells, in: Solar Cells and Light Management, Elsevier, 2020, pp. 163–228, https://doi.org/10.1016/B978-0-08-102762-2.00005-7.
[2] Z.-K. Tang, Z.-F. Xu, D.-Y. Zhang, S.-X. Hu, W.-M. Lau, L.-M. Liu, Enhanced optical absorption via cation doping hybrid lead iodine perovskites, Sci. Rep. 7 (2017) 7843, https://doi.org/10.1038/s41598-017-08215-3.
[3] P. Azarhoosh, S. McKechnie, J.M. Frost, A. Walsh, M. van Schilfgaarde, Research Update: relativistic origin of slow electron-hole recombination in hybrid halide perovskite solar cells, Apl. Mater. 4 (2016) 091501, https://doi.org/10.1063/1.4955028.
[4] C. Motta, F. El-Mellouhi, S. Sanvito, Charge carrier mobility in hybrid halide perovskites, Sci. Rep. (2015), https://doi.org/10.1038/srep12746.
[5] S. Razza, S. Castro-Hermosa, A. Di Carlo, T.M. Brown, Research Update: large-area deposition, coating, printing, and processing techniques for the upscaling of perovskite solar cell technology, Apl. Mater. (2016), https://doi.org/10.1063/1.4962478.
[6] X. Peng, J. Yuan, S. Shen, M. Gao, A.S.R. Chesman, H. Yin, J. Cheng, Q. Zhang, D. Angmo, Perovskite and organic solar cells fabricated by inkjet printing: progress and prospects, Adv. Funct. Mater. (2017), https://doi.org/10.1002/adfm.201703704.
[7] M. Cai, Y. Wu, H. Chen, X. Yang, Y. Qiang, L. Han, Cost-performance analysis of perovskite solar modules, Adv. Sci. (2017), https://doi.org/10.1002/advs.201600269.
[8] https://www.nrel.gov/pv/assets/images/cell-pv-eff-emergingpv.jpg, 2024.
[9] B. Chen, P.N. Rudd, S. Yang, Y. Yuan, J. Huang, Imperfections and their passivation in halide perovskite solar cells, Chem. Soc. Rev. (2019), https://doi.org/10.1039/c8cs00853a.
[10] S. Cacovich, L. Ciná, F. Matteocci, G. Divitini, P.A. Midgley, A. Di Carlo, C. Ducati, T.M. Brown, A. Reale, A. Di Carlo, Gold and iodine diffusion in large area perovskite solar cells under illumination, Nanoscale 9 (2017) 4700–4706, https://doi.org/10.1039/C7NR00784A.
[11] W. Li, J. Liu, F.-Q. Bai, H.-X. Zhang, O.V. Prezhdo, Hole trapping by iodine interstitial defects decreases free carrier losses in perovskite solar cells: a time-domain *Ab Initio* study, ACS Energy Lett. 2 (2017) 1270–1278, https://doi.org/10.1021/acsenergylett.7b00183.
[12] G.M. Whitesides, B. Grzybowski, Self-assembly at all scales, Science 295 (2002) (1979) 2418–2421, https://doi.org/10.1126/science.1070821.
[13] S. Zhang, Fabrication of novel biomaterials through molecular self-assembly, Nat. Biotechnol. 21 (2003) 1171–1178, https://doi.org/10.1038/nbt874.
[14] S. Casalini, C.A. Bortolotti, F. Leonardi, F. Biscarini, Self-assembled monolayers in organic electronics, Chem. Soc. Rev. 46 (2017) 40–71, https://doi.org/10.1039/C6CS00509H.
[15] G. Sathiyan, H. Wang, C. Chen, Y. Miao, M. Zhai, M. Cheng, Impact of fluorine substitution in organic functional materials for perovskite solar cell, Dyes Pigments. 198 (2022) 110029, https://doi.org/10.1016/j.dyepig.2021.110029.
[16] M. Hossain, R. Garai, R.K. Gupta, R.N. Arunagirinathan, P.K. Iyer, Fluoroarene derivative based passivation of perovskite solar cells exhibiting excellent ambient and thermo-stability achieving efficiency >20, J Mater Chem C Mater. 9 (2021) 10406–10413, https://doi.org/10.1039/D1TC02335G.
[17] Z. Yi, X. Li, Y. Xiong, G. Shen, W. Zhang, Y. Huang, Q. Jiang, X.R. Ng, Y. Luo, J. Zheng, W.L. Leong, F. Fu, T. Bu, J. Yang, Self-assembled monolayers (SAMs) in inverted perovskite solar cells and their tandem photovoltaics application, Interdisciplinary Materials. 3 (2024) 203–244, https://doi.org/10.1002/idm2.12145.
[18] J.-W.A. Schüttauf, K.H.M. van der Werf, I.M. Kielen, W.G.J.H.M. van Sark, J. K. Rath, R.E.I. Schropp, Excellent crystalline silicon surface passivation by

amorphous silicon irrespective of the technique used for chemical vapor deposition, Appl. Phys. Lett. 98 (2011), https://doi.org/10.1063/1.3579540.
[19] J. Peng, J.I. Khan, W. Liu, E. Ugur, T. Duong, Y. Wu, H. Shen, K. Wang, H. Dang, E. Aydin, X. Yang, Y. Wan, K.J. Weber, K.R. Catchpole, F. Laquai, S. De Wolf, T. P. White, A universal double-side passivation for high open-circuit voltage in perovskite solar cells: role of carbonyl groups in poly(methyl methacrylate), Adv. Energy Mater. 8 (2018), https://doi.org/10.1002/aenm.201801208.
[20] J. Kim, Y.R. Kim, J. Kim, C. Oh, I. Hwang, J. Kim, S. Zeiske, T. Ki, S. Kwon, H. Kim, A. Armin, H. Suh, K. Lee, Efficient and stable perovskite solar cells with a high open-circuit voltage over 1.2 V achieved by a dual-side passivation layer, Adv. Mater. 34 (2022), https://doi.org/10.1002/adma.202205268.
[21] B. Kim, B. Gil, S. Ryu, J. Kim, B. Park, Double-side passivation of perovskite solar cells for high performance and stability, Adv. Funct. Mater. 33 (2023), https://doi.org/10.1002/adfm.202307640.
[22] M.A. Mahmud, T. Duong, Y. Yin, H.T. Pham, D. Walter, J. Peng, Y. Wu, L. Li, H. Shen, N. Wu, N. Mozaffari, G. Andersson, K.R. Catchpole, K.J. Weber, T. P. White, Double-sided surface passivation of 3D perovskite film for high-efficiency mixed-dimensional perovskite solar cells, Adv. Funct. Mater. 30 (2020), https://doi.org/10.1002/adfm.201907962.
[23] P.K. Sukhorukova, E.A. Ilicheva, P.A. Gostishchev, L.O. Luchnikov, M. M. Tepliakova, D.O. Balakirev, I.V. Dyadishchev, A.A. Vasilev, D.S. Muratov, D. A. Kiselev, T.S. Ilina, YuN. Luponosov, A. Di Carlo, D.S. Saranin, Triphenylamine-based interlayer with carboxyl anchoring group for tuning of charge collection interface in stabilized p-i-n perovskite solar cells and modules, J. Power Sources 604 (2024) 234436, https://doi.org/10.1016/j.jpowsour.2024.234436.
[24] X. Huang, C. Liang, H. Gong, C. Zhang, X. Guo, D. Li, F. You, Z. He, 2D/3D heterojunction engineering at the grain boundaries towards high-performance inverted MA-free perovskite solar cells, Org. Electron. 122 (2023) 106918, https://doi.org/10.1016/j.orgel.2023.106918.
[25] A. Amat, E. Mosconi, E. Ronca, C. Quarti, P. Umari, MdK. Nazeeruddin, M. Grätzel, F. De Angelis, Cation-induced band-gap tuning in organohalide perovskites: interplay of spin–orbit coupling and octahedra tilting, Nano Lett. 14 (2014) 3608–3616, https://doi.org/10.1021/nl5012992.
[26] P. Gostishchev, D. Saranin, L. Luchnikov, D. Muratov, A. Ishteev, M. Voronova, D. Gets, E. Argunov, T.S. Le, S. Didenko, A. Di Carlo, Cl-Anion engineering for halide perovskite solar cells and modules with enhanced photostability, Sol. RRL 7 (2023) 2200941, https://doi.org/10.1002/solr.202200941.
[27] V. Campanari, F. Martelli, A. Agresti, S. Pescetelli, N.Y. Nia, F. Di Giacomo, D. Catone, P. O'Keeffe, S. Turchini, B. Yang, J. Suo, A. Hagfeldt, A. Di Carlo, Reevaluation of photoluminescence intensity as an indicator of efficiency in perovskite solar cells, Sol. RRL 6 (2022), https://doi.org/10.1002/solr.202200049.
[28] D.S. Saranin, V.N. Mazov, L.O. Luchnikov, D.A. Lypenko, P.A. Gostishev, D. S. Muratov, D.A. Podgorny, D.M. Migunov, S.I. Didenko, M.N. Orlova, D. V. Kuznetsov, A.R. Tameev, A. Di Carlo, Tris(ethylene diamine) nickel acetate as a promising precursor for hole transport layer in planar structured perovskite solar cells, J Mater Chem C Mater. 6 (2018), https://doi.org/10.1039/c8tc01169a.
[29] J. Guo, B. Wang, D. Lu, T. Wang, T. Liu, R. Wang, X. Dong, T. Zhou, N. Zheng, Q. Fu, Z. Xie, X. Wan, G. Xing, Y. Chen, Y. Liu, Ultralong carrier lifetime exceeding 20 μs in lead halide perovskite film enable efficient solar cells, Adv. Mater. 35 (2023), https://doi.org/10.1002/adma.202212126.
[30] J. Jiang, X. Sun, X. Chen, B. Wang, Z. Chen, Y. Hu, Y. Guo, L. Zhang, Y. Ma, L. Gao, F. Zheng, L. Jin, M. Chen, Z. Ma, Y. Zhou, N.P. Padture, K. Beach, H. Terrones, Y. Shi, D. Gall, T.-M. Lu, E. Wertz, J. Feng, J. Shi, Carrier lifetime enhancement in halide perovskite via remote epitaxy, Nat. Commun. 10 (2019) 4145, https://doi.org/10.1038/s41467-019-12056-1.
[31] J. Zhao, Y. Deng, H. Wei, X. Zheng, Z. Yu, Y. Shao, J.E. Shield, J. Huang, Strained hybrid perovskite thin films and their impact on the intrinsic stability of perovskite solar cells, Sci. Adv. 3 (2017) 1–8, https://doi.org/10.1126/sciadv.aao5616.
[32] J. Hu, Z. Xu, T.L. Murrey, I. Pelczer, A. Kahn, J. Schwartz, B.P. Rand, Triiodide attacks the organic cation in hybrid lead halide perovskites: mechanism and suppression, Adv. Mater. 35 (2023), https://doi.org/10.1002/adma.202303373.
[33] A.A. Ordinartsev, A.A. Petrov, K.A. Lyssenko, A.V. Petrov, E.A. Goodilin, A. B. Tarasov, Crystal structure of new formamidinium triiodide jointly refined by single-crystal XRD, Raman scattering spectroscopy and DFT assessment of hydrogen-bond network features, Acta Crystallogr E Crystallogr Commun. 77 (2021) 692–695, https://doi.org/10.1107/S2056989021005673.
[34] C. Liu, Y. Yang, H. Chen, J. Xu, A. Liu, A.S.R. Bati, H. Zhu, L. Grater, S.S. Hadke, C. Huang, V.K. Sangwan, T. Cai, D. Shin, L.X. Chen, M.C. Hersam, C.A. Mirkin, B. Chen, M.G. Kanatzidis, E.H. Sargent, Bimolecularly passivated interface enables efficient and stable inverted perovskite solar cells, Science 382 (2023) (1979) 810–815, https://doi.org/10.1126/science.adk1633.
[35] Y. Tong, G.R. Berdiyorov, A. Sinopoli, M.E. Madjet, V.A. Esaulov, H. Hamoudi, An estimation on the mechanical stabilities of SAMs by low energy Ar+ cluster ion collision, Sci. Rep. 11 (2021) 12772, https://doi.org/10.1038/s41598-021-92077-3.
[36] T. Golubev, D. Liu, R. Lunt, P. Duxbury, Understanding the impact of C60 at the interface of perovskite solar cells via drift-diffusion modeling, AIP Adv. 9 (2019), https://doi.org/10.1063/1.5068690.
[37] R.S. Sanchez, V. Gonzalez-Pedro, J.-W. Lee, N.-G. Park, Y.S. Kang, I. Mora-Sero, J. Bisquert, Slow dynamic processes in lead halide perovskite solar cells. Characteristic times and hysteresis, J. Phys. Chem. Lett. 5 (2014) 2357–2363, https://doi.org/10.1021/jz5011187.
[38] D. Di Girolamo, F. Di Giacomo, F. Matteocci, A.G. Marrani, D. Dini, A. Abate, Progress, highlights and perspectives on NiO in perovskite photovoltaics, Chem. Sci. 11 (2020) 7746–7759, https://doi.org/10.1039/D0SC02859B.
[39] C. Gonzales, A. Guerrero, J. Bisquert, Transition from capacitive to inductive hysteresis: a neuron-style model to correlate $I - V$ curves to impedances of metal halide perovskites, J. Phys. Chem. C. 126 (2022) 13560–13578, https://doi.org/10.1021/acs.jpcc.2c02729.
[40] M. Ahmadi, T. Wu, B. Hu, A review on organic–inorganic halide perovskite photodetectors: device engineering and fundamental physics, Adv. Mater. 29 (2017), https://doi.org/10.1002/adma.201605242.
[41] M.V. Khenkin, E.A. Katz, A. Abate, G. Bardizza, J.J. Berry, C. Brabec, F. Brunetti, V. Bulović, Q. Burlingame, A. Di Carlo, R. Cheacharoen, Y.B. Cheng, A. Colsmann, S. Cros, K. Domanski, M. Dusza, C.J. Fell, S.R. Forrest, Y. Galagan, D. Di Girolamo, M. Grätzel, A. Hagfeldt, E. von Hauff, H. Hoppe, J. Kettle, H. Köbler, M.S. Leite, S. Frank, Liu, Y.L. Loo, J.M. Luther, C.Q. Ma, M. Madsen, M. Manceau, M. Matheron, M. McGehee, R. Meitzner, M.K. Nazeeruddin, A.F. Nogueira, Ç. Odabaşı, A. Osherov, N.G. Park, M.O. Reese, F. De Rossi, M. Saliba, U. S. Schubert, H.J. Snaith, S.D. Stranks, W. Tress, P.A. Troshin, V. Turkovic, S. Veenstra, I. Visoly-Fisher, A. Walsh, T. Watson, H. Xie, R. Yıldırım, S. M. Zakeeruddin, K. Zhu, M. Lira-Cantu, Consensus statement for stability assessment and reporting for perovskite photovoltaics based on ISOS procedures, Nat. Energy (2020), https://doi.org/10.1038/s41560-019-0529-5.
[42] V.L. Pool, B. Dou, D.G. Van Campen, T.R. Klein-Stockert, F.S. Barnes, S.E. Shaheen, M.I. Ahmad, M.F.A.M. van Hest, M.F. Toney, Thermal engineering of FAPbI3 perovskite material via radiative thermal annealing and in situ XRD, Nat. Commun. 8 (2017) 14075, https://doi.org/10.1038/ncomms14075.
[43] J. Zhou, Z. Liu, P. Yu, G. Tong, R. Chen, L.K. Ono, R. Chen, H. Wang, F. Ren, S. Liu, J. Wang, Z. Lan, Y. Qi, W. Chen, Modulation of perovskite degradation with multiple-barrier for light-heat stable perovskite solar cells, Nat. Commun. 14 (2023) 6120, https://doi.org/10.1038/s41467-023-41856-9.
[44] N.N. Udalova, E.M. Nemygina, E.A. Zharenova, A.S. Tutantsev, A.A. Sudakov, A. Y. Grishko, N.A. Belich, E.A. Goodilin, A.B. Tarasov, New aspects of copper electrode metamorphosis in perovskite solar cells, J. Phys. Chem. C 124 (2020) 24601–24607, https://doi.org/10.1021/ACS.JPCC.0C06608/SUPPL_FILE/JP0C06608_SI_001.PDF.
[45] S. Yang, J. Dai, Z. Yu, Y. Shao, Y. Zhou, X. Xiao, X.C. Zeng, J. Huang, Tailoring passivation molecular structures for extremely small open-circuit voltage loss in perovskite solar cells, J. Am. Chem. Soc. 141 (2019) 5781–5787, https://doi.org/10.1021/jacs.8b13091.
[46] S. Mariotti, I.N. Rabehi, C. Zhang, X. Huo, J. Zhang, P. Ji, T. Wu, T. Li, S. Yuan, X. Liu, T. Guo, C. Ding, H. Wang, A. Bruno, L.K. Ono, Y. Qi, Unraveling the morphological and energetic properties of <scp>2PACz</scp> self-assembled monolayers fabricated with upscaling deposition methods, Energy Environ. Mater. (2024), https://doi.org/10.1002/eem2.12825.
[47] D.S. Mann, S. Thakur, S.S. Sangale, K.-U. Jeong, S.-N. Kwon, S.-I. Na, Antisolvent additive engineering containing green additive for efficient and stable perovskite solar cells, Sol. Energy Mater. Sol. Cell. 269 (2024) 112768, https://doi.org/10.1016/j.solmat.2024.112768.
[48] S. Zhang, R. Wu, C. Mu, Y. Wang, L. Han, Y. Wu, W.-H. Zhu, Conjugated self-assembled monolayer as stable hole-selective contact for inverted perovskite solar cells, ACS Mater. Lett. 4 (2022) 1976–1983, https://doi.org/10.1021/acsmaterialslett.2c00799.
[49] S. Wang, H. Guo, Y. Wu, Advantages and challenges of self-assembled monolayer as a hole-selective contact for perovskite solar cells, Materials Futures. 2 (2023) 012105, https://doi.org/10.1088/2752-5724/acbb5a.
[50] A. Al-Ashouri, A. Magomedov, M. Roß, M. Jošt, M. Talaikis, G. Chistiakova, T. Bertram, J.A. Márquez, E. Köhnen, E. Kasparavičius, S. Levcenco, L. Gil-Escrig, C.J. Hages, R. Schlatmann, B. Rech, T. Malinauskas, T. Unold, C.A. Kaufmann, L. Korte, G. Niaura, V. Getautis, S. Albrecht, Conformal monolayer contacts with lossless interfaces for perovskite single junction and monolithic tandem solar cells, Energy Environ. Sci. 12 (2019) 3356–3369, https://doi.org/10.1039/C9EE02268F.
[51] Q. Jiang, K. Zhu, Rapid advances enabling high-performance inverted perovskite solar cells, Nat. Rev. Mater. 9 (2024) 399–419, https://doi.org/10.1038/s41578-024-00678-x.
[52] M. Hatamvand, S. Gholipour, M. Chen, Y. Zhou, T. Jiang, Z. Hu, Y. Chen, W. Huang, Dual-side interfacial passivation of FAPbI3 perovskite film by Naphthylmethylammonium iodide for highly efficient and stable perovskite solar cells, Chem. Eng. J. 460 (2023) 141788, https://doi.org/10.1016/j.cej.2023.141788.
[53] R. Azmi, D.S. Utomo, B. Vishal, S. Zhumagali, P. Dally, A.M. Risqi, A. Prasetio, E. Ugur, F. Cao, I.F. Imran, A.A. Said, A.R. Pininti, A.S. Subbiah, E. Aydin, C. Xiao, S. Il Seok, S. De Wolf, Double-side 2D/3D heterojunctions for inverted perovskite solar cells, Nature 628 (2024) 93–98, https://doi.org/10.1038/s41586-024-07189-3.